Supplement of Atmos. Chem. Phys., 24, 1801–1824, 2024
https://doi.org/10.5194/acp-24-1801-2024-supplement

Atmospheric Chemistry and Physics
Open Access
EGU

Supplement of

Higher absorption enhancement of black carbon in summer shown by 2-year measurements at the high-altitude mountain site of Pic du Midi Observatory in the French Pyrenees

Sarah Tinorua et al.

Correspondence to: Sarah Tinorua (sarah.tinorua@umr-cnrm.fr) and Cyrielle Denjean (cyrielle.denjean@meteo.fr)

Supplement

S1: Data processing for retrieving SP2 mass concentrations

The Paul Scherrer Institute's SP2 toolkit is a softwave developed using IGOR to provide quantitative analysis of rBC mass concentration. However, this software is not suitable to analyze large amounts of data. During the PDM campaign, more than 1.2 To of data has been recorded. Processing it with the PSI toolkit would be too much time-consuming. This is why we developed a software on Python. The data analysis was validated by comparing our M_{rBC} to the one obtained by the SP2 toolkit.
Supplementary S1 presents a comparison between the M_{rBC} retrieved with our Python program in blue, and the M_{rBC} calculated with the PSI SP2 toolkit in red. The output M_{rBC} from the toolkit does not take into account the rBC mass fraction below and above the SP2 size detection range corresponding to $90 < D_{rBC} < 580$ nm. Therefore M_{rBC} without correction of the missing mass fraction is presented here. Globally over the 3 days, the two processing yielded M_{rBC} values in agreement taking into account the 14% of uncertainties on M_{rBC} (shaded areas), with a mean M_{rBC} of 101.1 ± 14.2 and 82.3 ± 11.5 ng m^{-3} for our method and the SP2 toolkit, respectively. The SP2 toolkit seems to generate more M_{rBC} peaks compared to our method, which smooths a bit more the time series. Such high peaks of M_{rBC} don't seem realistic, given the situation of the site (remote station, without the presence of local rBC sources). The values provided by the PSI toolkit may be more noisy than the Python software due to different filters applied to the individual signals, a difference in the flowrate sampling, or a different estimation of the baseline of the incandescence peak height, leading to bias in individual masses. These different possibilities have not been explored in detail.

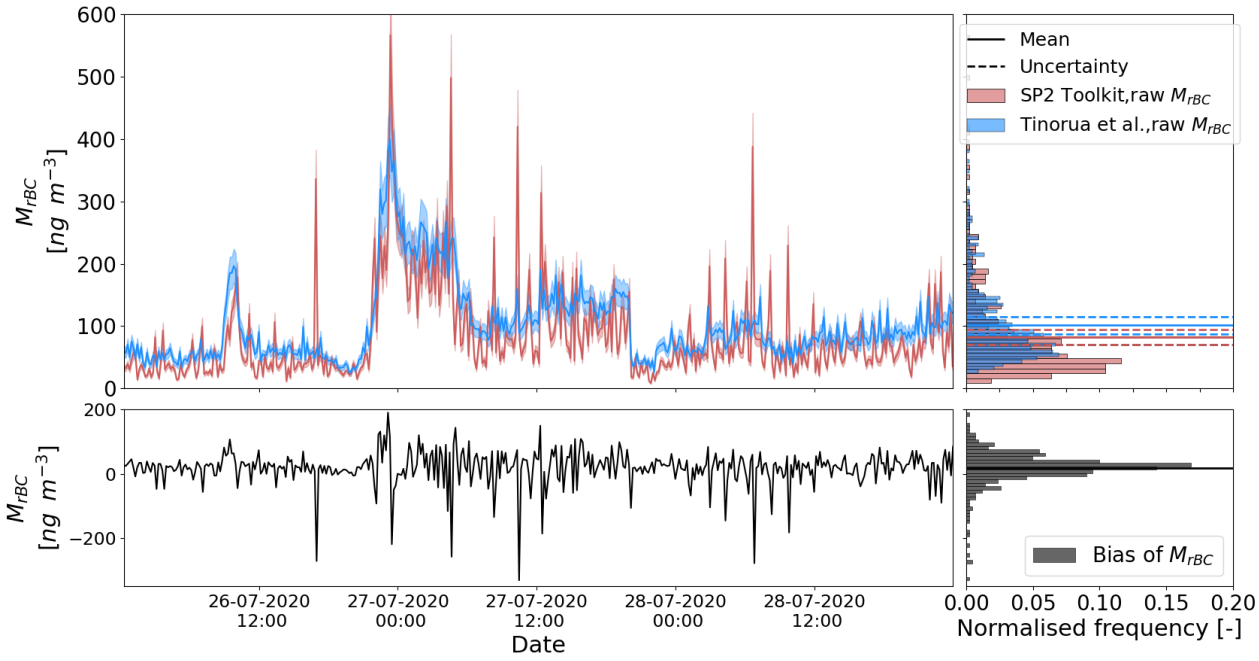

Figure S1: 72-h comparison between M_{rBC} calculated with the PSI SP2 toolkit and M_{rBC} calculated with the Python program developped in this study. Data was 10-min averaged on the period from 26th to 28th July, 2020.The top left panel shows M_{rBC} time series with the shaded area representing the M_{rBC} uncertainties, and the associated histogram on the right-hand side with the mean M_{rBC} and its uncertainties represented by the solid and dashed lines, respectively. The bottom panel shows the bias (M_{rBC} from our processing minus M_{rBC} from the SP2 toolkit) and its associated histogram on the right-hand side. M_{rBC} data was here measured for rBC cores between 90 to 580 nm, without correction of the missing mass fraction.

S2 : Information about the rBC size distribution processing

The SP2 measures rBC cores from mass equivalent diameters of 90 to 580 nm. Fig. S2 shows the two-year average of the daily rBC cores size distributions. It can be noticed in Fig. S2 that the number size distribution measured by the SP2 did not cover the full size range of rBC at PDM. This is particularly true for the rBC particles below 90 nm, where the major fraction of the M_{rBC} was missed by the SP2. In order to estimate the missing rBC mass fraction undetected by the SP2 (e.g. the mass size distribution under 90 nm and over 580 nm), the daily rBC mass size distributions were fitted with a sum of three lognormal functions as :

$$\frac{dM}{dln(D_p)} = \sum_{i=0}^{3} \left(\frac{M_i}{\sqrt{2\pi}\ln(\sigma_{g,i})} \exp\left[\frac{-\ln^2(D/D_{g,i})}{2\ln^2(\sigma_{g,i})} \right] \right)$$

with M_i, $D_{g,i}$ and $\sigma_{g,i}$ representing the rBC mass concentration, the geometric mean diameter and the geometric standard deviation of the mode i, respectively. The same function with two modes has been used to fit the number size distribution.

The fitting parameters were constrained in the following ranges : Mode 1 : $50 < D_{g,1} < 100$ nm and $1.2 < \sigma_{g,1} < 3$; Mode 2 : $150 < D_{g,2} < 250$ nm and $1.3 < \sigma_{g,2,} < 2.9$; Mode 3 : $350 < D_{g,3} < 500$ nm and $1 < \sigma_{g,3} < 3$.

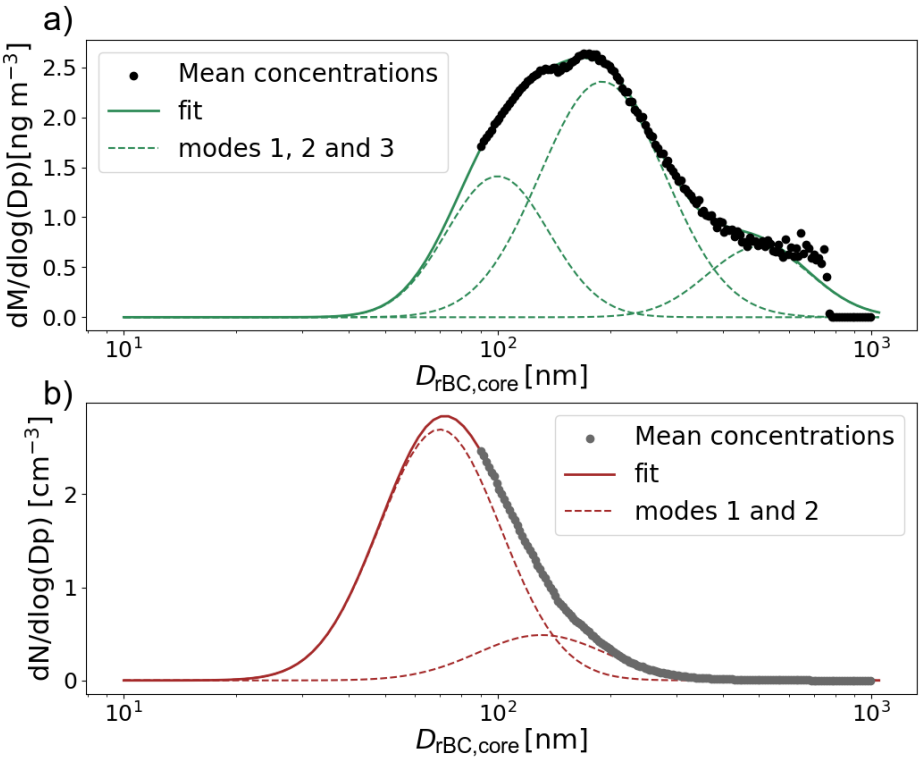

Figure S2: rBC core mass (top) and number (bottom) size distribution measured by the SP2 and fitted with a sum of three an two modes, respectively. Lognormal fits are overlaid in plain colored line with the three(respectively two) modes detailed in dashed colored lines.

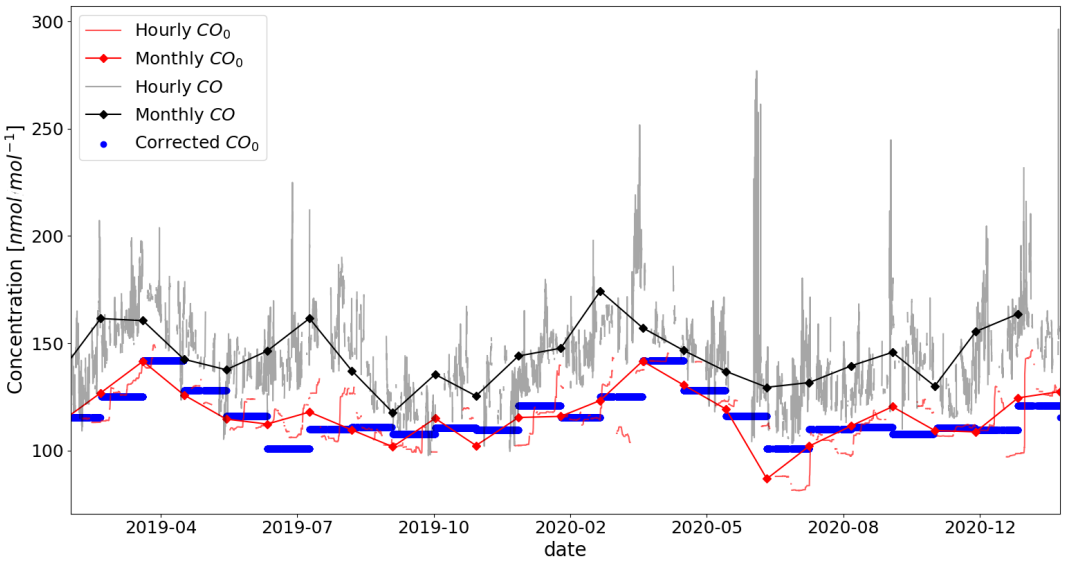

Figure S3: Determination of $\Delta M_{rBC}/\Delta CO$ emission ratios. Hourly background CO (red line) was calculated as the 14-day rolling 5th percentile of CO hourly concentrations (in gray). Then these values were averaged by months (red and blue dots)

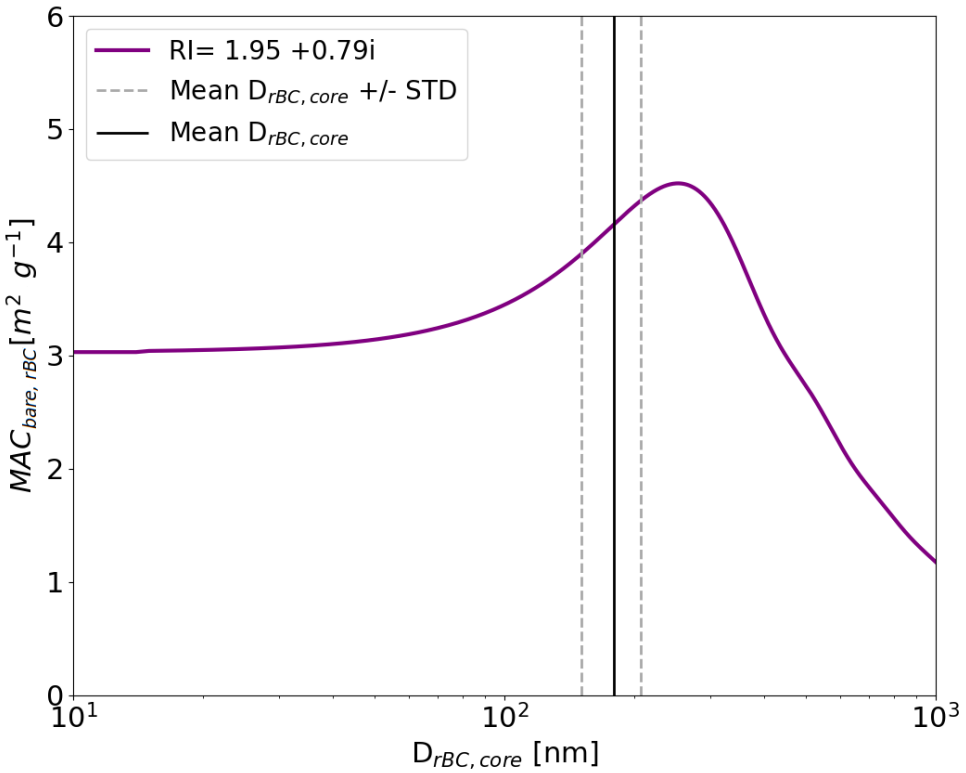

Figure S4: Bare rBC MAC calculation with Mie theory at 880 nm as a function of the rBC core diameter. Vertical solid and dashed lines are the mean $D_{rBC,core}$ and standard deviation, respectively. $MAC_{bare,rBC}$ has been calculated with a refractive index of 1.95 +0.79i.

S3: Discrimination of FT/PBL conditions with the radon activity data

In the present study, the method used to discriminate anabatic vs. non-anabatic days follows the method by Griffiths et al. (2014) based on radon measurements, and the recognition that the anabatic influence can be measured by the amplitude of a diurnal radon cycle, properly phased with a maximum in the afternoon. The method mainly consists in ranking days by decreasing anabatic influence. All details of the ranking algorithm are given in Griffiths et al. (2014), but in overview (citing the authors) "the procedure involves computing the diurnal composite of the set of all observed days and then removing days from the set in the order which most quickly reduces the mean square amplitude of the set's composite diurnal cycle."

In our study, the procedure to compute the ranking strictly follows the steps described in Griffiths et al. (2014), except on this only point: as input data for the ranking procedure, these authors use the absolute deviation between the hourly radon data and the daily mean of the current day. In our case, we alternatively used the relative deviation (i.e. the absolute deviation normalized by the current-day mean). This considerably improved the result because the radon regional background at PDM is suspected to be much more variable than at the Jungfraujoch (see discussion below).

Then, a diagnostic value called "anabatic radon" is calculated for each day, which represents (in short) the average deviation of radon above a nocturnal background (see full detail of the calculation in Griffiths et al. (2014), which we again strictly followed). Anabatic radon mostly decreases with increasing anabatic rank (Fig. S5), at least up to a threshold rank (282) corresponding to its first minimum. The inserted graph in Fig. S5 shows that the amplitude of the diurnal composite of radon activity decreases with increasing anabatic rank. Days ranked before this threshold are considered as anabatically-influenced (or more simply called "anabatic days"), and the days after this rank are considered as non-anabatic.

After this rank, anabatic radon values should expectedly be zero. This is obviously the case neither in Fig. S5, nor in the similar graph by Griffiths et al. (2014 – their Fig.3). The reason is that intraday radon variations due to any reason but anabatic transport, may occur out of phase with the thermally-driven cycle. Because of incoherent phasing, such variations contribute little to the set's composite diurnal cycle, and as a consequence, such days appear far in the ranking. But such variations may nevertheless be above the background (i.e. the minimum value) of the current day, and produce non negligible values of the "anabatic radon" diagnostic – which has thus little sense for non anabatic days.

A question arises, however, why anabatic radon appear more noisy in our Fig. S5 than in the similar graph in Griffiths et al. (their Fig.3). We have no definitive explanation to this, but may speculate that radon sources at the regional scale around Pic du Midi are more heterogeneous and intense than around the Jungfraujoch. Supporting this idea are radon exhalation maps by soils presented in (Karstens et al. (2015) or (Quérel et al. (2022), showing radon hot spots in the western Iberian peninsula, in the French Massif Central, and (to a lesser extent) locally in the Pyrenees. In such conditions, the radon background at Pic du Midi may be much more variable than at JFJ, and other transport processes than anabatic transport may thus contribute more strongly to radon variability at PDM. This would deserve specific investigation, but is out of the scope of the present study.

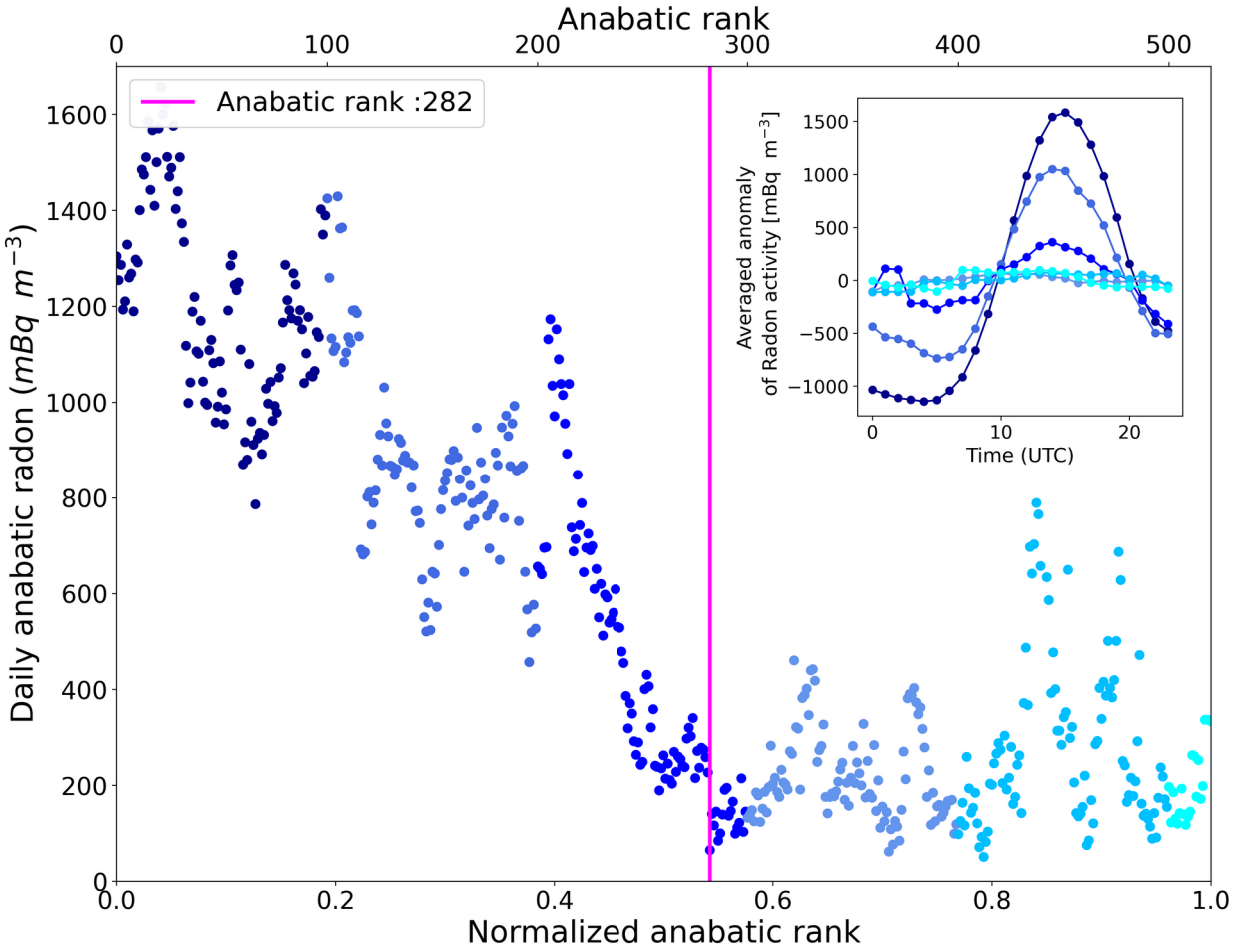

Figure S5: Daily anabatic radon as a function of the day anabatic rank (see text for details). Each dot represent an observation day ranked from the most anabatically-influenced day (left) to the least one (right). The vertical pink line represents the cut-off rank before which days can be considered as PBL-influenced. The insert shows diurnal composites of radon activity anomaly according to different ranges of ranks, using the same color code as in the main plot.

S4 : Description of the meteorological variability at PDM

The meteorological conditions at PDM during the campaign were characterized by a strong seasonal trend of temperatures, with daily means ranging between -15 and +15°C (Fig. S6). The time series of relative humidity (RH) covered a wide range between 5 % and 100 % with an annual mean value of 71.2 %. Lower ambient RH was observed in summer compared to winter with median values of 67 % and 78 %, respectively. Irrespective of the season, the wind direction was dominated by westerly and south-westerly winds and a median speed of 7 m s^{-1}.

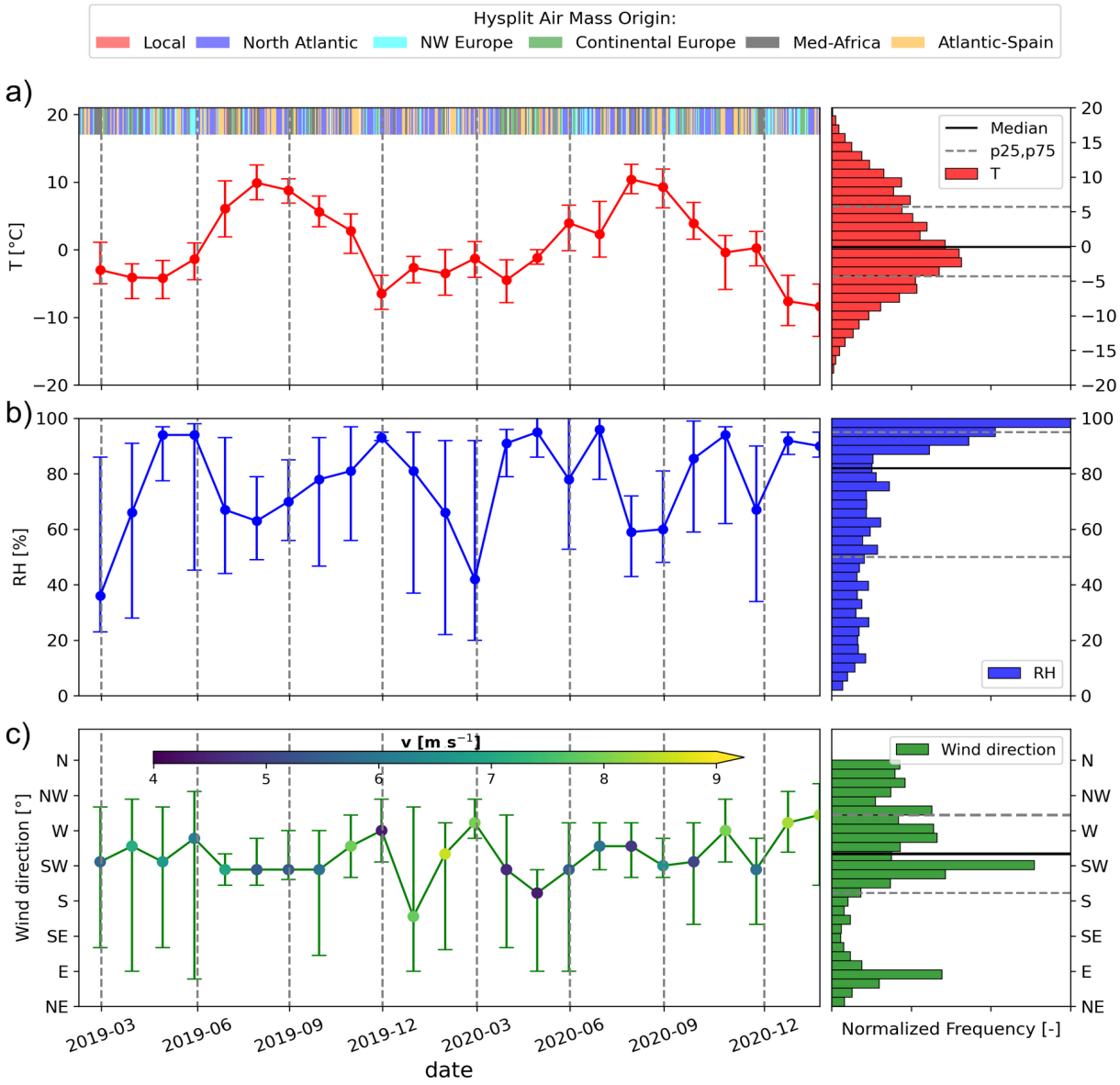

Figure S6: Time series (left) and statistical distributions (median, 25th and 75th percentiles, right) of meteorological parameters measured at PDM in 2019-2020 with (a) the temperature and Hysplit air mass origin, (b) the relative humidity and (c) the wind direction and speed. The dots and bars on the time series represent the median, the 25th and 75th percentiles, respectively, with a monthly frequency. Histograms was computed using a 1-day time frequency. Vertical dashed lines represent the seasons boundaries.

Table S1 : Statistics of BL/FT cases determination at PDM

	All the campaign	Winter	Summer
FT conditions (h)	1149	294	293
BL influence (h)	894	105	318
%age of FT influence	56.2	73.2	47.9

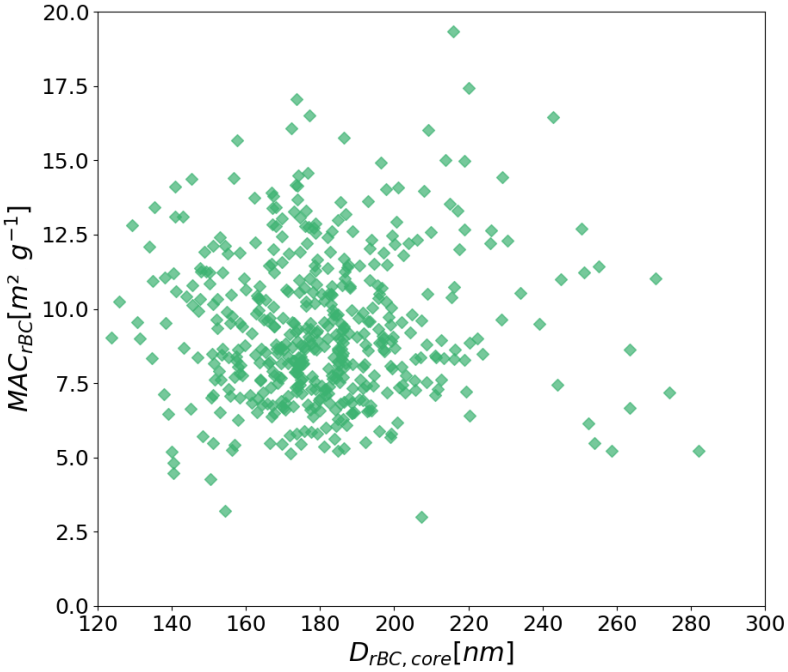

Figure S7: MAC_{rBC} as a function of $D_{rBC,core}$ over the campaign. Each point represents 1 day average data.

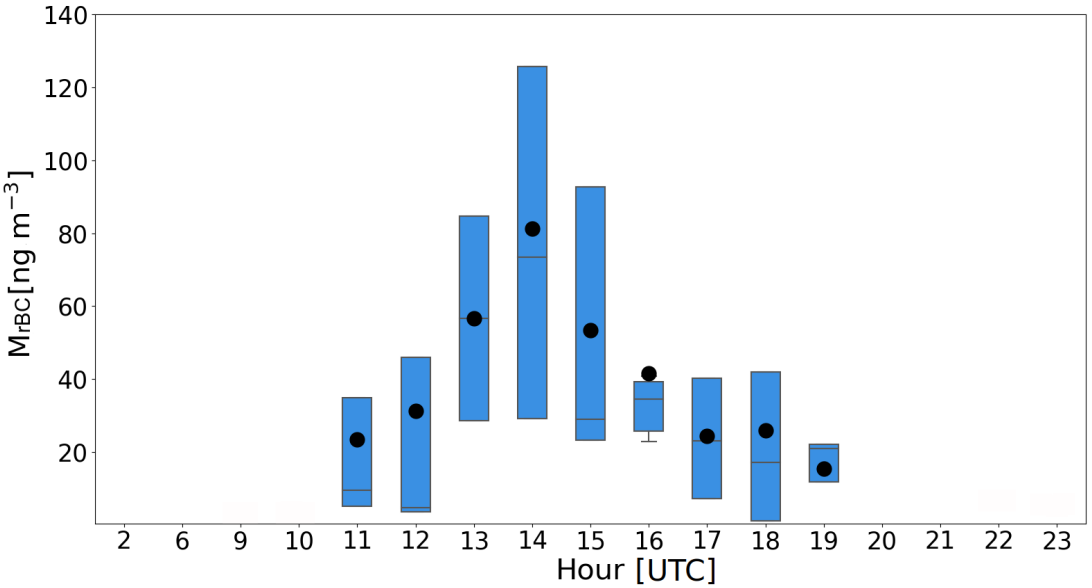

Figure S8: Hourly variation of rBC mass concentration in winter under PBL-influenced conditions. Statistics of the boxplot are the same as Fig. 7. Times without boxplot are due to the selected PBL-influenced hours, which are mostly during the daytime.

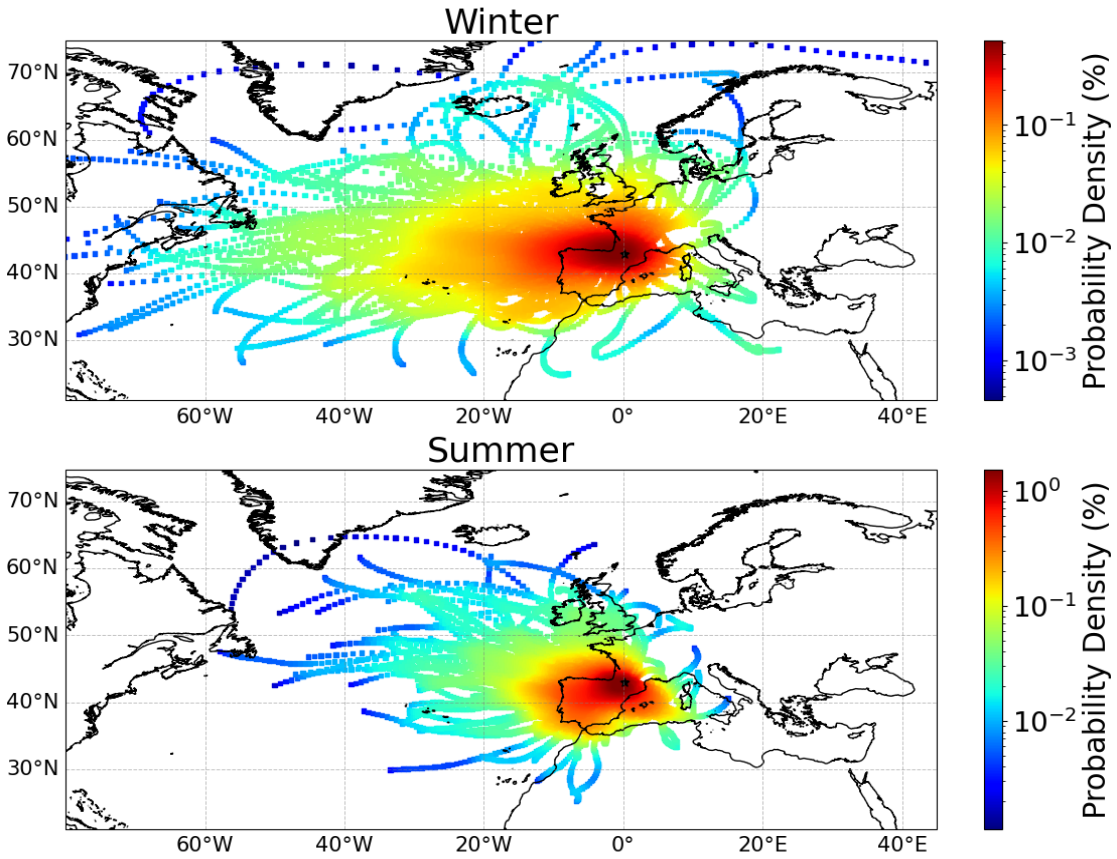

Figure S9: Computed density of airmass backtrajectories reaching PDM during the campaign calculated with the HYSPLIT model for winter and summer.

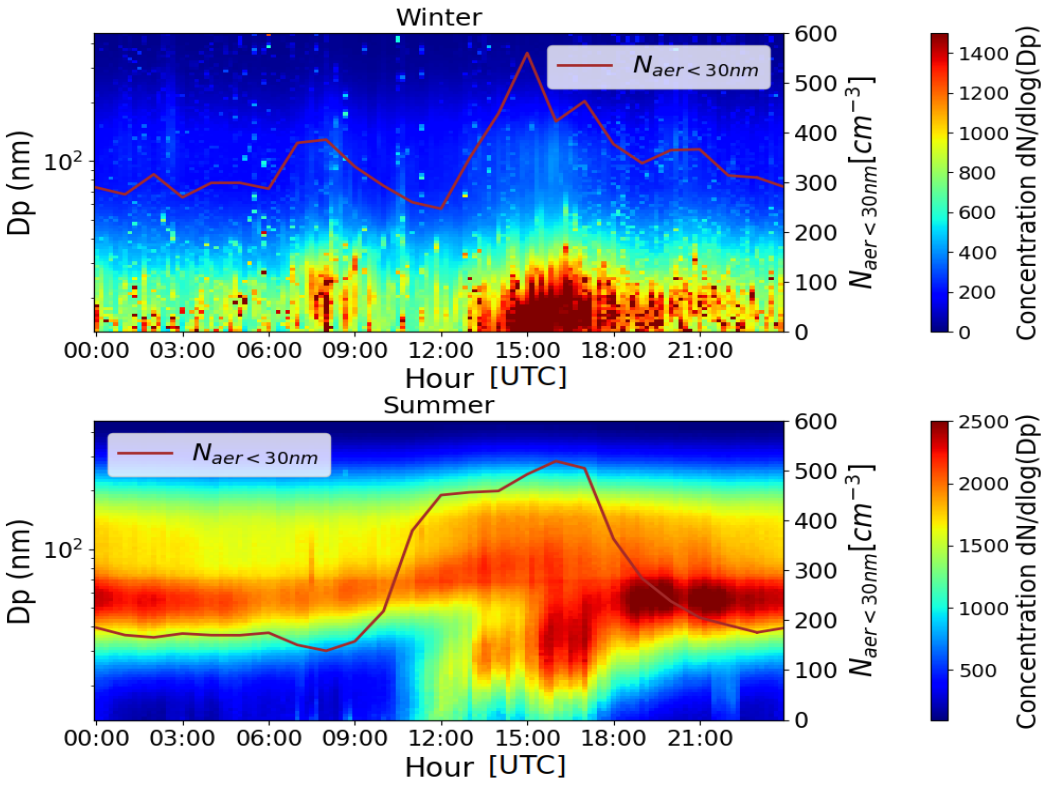

Figure S10: Average diurnal cycle of aerosols number size distribution in (a) winter and (b) summer. Number concentrations of the lower Aïtken mode (<30nm) are overlaid in red.

References:

Bukowiecki, N., Weingartner, E., Gysel, M., Coen, M. C., Zieger, P., Herrmann, E., Steinbacher, M., Ga¨ggeler, H. W., and Baltensperger, U.: A Review of More than 20 Years of Aerosol Observation at the High Altitude Research Station Jungfraujoch, Switzerland (3580 m asl), Aerosol and Air Quality Research, 16, 764–788, https://doi.org/10.4209/aaqr.2015.05.0305, publisher: Taiwan Association for Aerosol Research, 2016.

Griffiths, A. D., Conen, F., Weingartner, E., Zimmermann, L., Chambers, S. D., Williams, A. G., & Steinbacher, M. (2014). Surface-to-mountaintop transport characterised by radon observations at the Jungfraujoch. *Atmospheric Chemistry and Physics*, *14*(23), 12763-12779. https://doi.org/10.5194/acp-14-12763-2014

Karstens, U., Schwingshackl, C., Schmithüsen, D., & Levin, I. (2015). A process-based ^{222}radon flux map for Europe and its comparison to long-term observations. *Atmospheric Chemistry and Physics*, *15*(22), 12845-12865. https://doi.org/10.5194/acp-15-12845-2015

Laj, P., Bigi, A., Rose, C., Andrews, E., Lund Myhre, C., Collaud Coen, M., Lin, Y., Wiedensohler, A., Schulz, M., Ogren, J. A., Fiebig, M., Gliß, J., Mortier, A., Pandolfi, M., Petäja, T., Kim, S.-W., Aas, W., Putaud, J.-P., Mayol-Bracero, O., Keywood, M., Labrador, L., Aalto, P., Ahlberg, E., Alados Arboledas, L., Alastuey, A., Andrade, M., Artíñano, B., Ausmeel, S., Arsov, T., Asmi, E., Backman, J., Baltensperger, U., Bastian, S., Bath, O., Beukes, J. P., Brem, B. T., Bukowiecki, N., Conil, S., Couret, C., Day, D., Dayantolis, W., Degorska, A., Eleftheriadis, K., Fetfatzis, P., Favez, O., Flentje, H., Gini, M. I., Gregorič, A., Gysel-Beer, M., Hallar, A. G., Hand, J., Hoffer, A., Hueglin, C., Hooda, R. K., Hyvärinen, A., Kalapov, I., Kalivitis, N., Kasper-Giebl, A., Kim, J. E., Kouvarakis, G., Kranjc, I., Krejci, R., Kulmala, M., Labuschagne, C., Lee, H.-J., Lihavainen, H., Lin, N.-H., Löschau, G., Luoma, K., Marinoni, A., Martins Dos Santos, S., Meinhardt, F., Merkel, M., Metzger, J.-M., Mihalopoulos, N., Nguyen, N. A., Ondracek, J., Pérez, N., Perrone, M. R., Petit, J.-E., Picard, D., Pichon, J.-M., Pont, V., Prats, N., Prenni, A., Reisen, F., Romano, S., Sellegri, K., Sharma, S., Schauer, G., Sheridan, P., Sherman, J. P., Schütze, M., Schwerin, A., Sohmer, R., Sorribas, M., Steinbacher, M., Sun, J., Titos, G., Toczko, B., Tuch, T., Tulet, P., Tunved, P., Vakkari, V., Velarde, F., Velasquez, P., Villani, P., Vratolis, S., Wang, S.-H., Weinhold, K., Weller, R., Yela, M., Yus-Diez, J., Zdimal, V., Zieger, P., and Zikova, N.: A global analysis of climate-relevant aerosol properties retrieved from the network of Global Atmosphere Watch (GAW) near-surface observatories, Atmospheric Measurement Techniques, 13, 4353–4392, https://doi.org/10.5194/amt-13-4353-2020, publisher: Copernicus GmbH, 2020.

Pandolfi, M., Ripoll, A., Querol, X., and Alastuey, A.: Climatology of aerosol optical properties and black carbon mass absorption cross section at a remote high-altitude site in the western Mediterranean Basin, Atmospheric Chemistry and Physics, 14, 6443–6460, https://doi.org/10.5194/acp-14-6443-2014, publisher: Copernicus GmbH, 2014.

Quérel, A., Meddouni, K., Quélo, D., Doursout, T., & Chuzel, S. (2022). Statistical approach to assess radon-222 long-range atmospheric transport modelling and its associated gamma dose rate peaks. *Advances in Geosciences*, *57*, 109-124. https://doi.org/10.5194/adgeo-57-109-2022